

The role of rifting in the development of the continental margins of the southwest subbasin, South China Sea: Insights from an OBS experiment

Chuanchuan Lü¹  · Tianyao Hao¹ · Jian Lin² · Xuelin Qiu³

Received: 21 June 2016 / Accepted: 15 November 2016 / Published online: 26 November 2016
© Springer Science+Business Media Dordrecht 2016

Abstract The continental margins of the southwest subbasin in the South China Sea mark a unique transition from multi-stages magma-poor continental rifting to seafloor spreading. We used reflection and refraction profiles across the margins to investigate the rifting process of the crust. Combining with the other seismic profiles acquired earlier, we focused on the comparative geological interpretation from the result of multichannel seismic analysis and wide-angle seismic tomography. Our result provides the evidence of upper crustal layer with abundant fractures below the acoustic basement with a P-wave velocity from 4.0 to 5.5 km s⁻¹. It indicates extensive deformation of the brittle crust during the continental rifting and can make a good explanation for the observed extension discrepancy in the rift margins of the South China Sea. The seismic chronostratigraphic result shows the possibility of the intra-continental extension center stayed focused for quite a long time in Eocene. Additionally, our evidence suggested that continental margin of the southwest subbasin had experienced at least three rifting stages and the existence of the

rigid blocks is an appropriate explanation to the asymmetric rifting of the South China Sea.

Keywords South China Sea · Southwest subbasin · Magma-poor rifted margins · Hyper-extended crust · Wide-angle reflection and refraction

Introduction

Before the oceanic crust accretion of the South China Sea (SCS), the passive margins of the SCS experienced progressive rifting starting from the early Paleocene (Taylor and Hayes 1983; Ru and Pigott 1986; Cullen et al. 2010; Franke 2013). As a consequence, an ultra-wide attenuated continental crust progressively dislocated from the South China continent and was rifted where a series of marginal basins formed within (Buck 1991; Clift and Lin 2001; Huismans and Beaumont 2008; Hall 2009; Franke et al. 2014). Additionally, as there is no evidence of salt or a Seaward Dipping Reflector, the margins of the SCS have been categorized as magma-poor rifted margins (Nissen et al. 1995; Qiu et al. 2001, 2011; Yan et al. 2001; Clift et al. 2002; McIntosh et al. 2005; Wang et al. 2006a; Lü et al. 2011; Ruan et al. 2011; Pichot et al. 2014). Unlike the classic magma-poor margins of the Iberia-Newfoundland margins (Ranero and Pérez-Gussinyé 2010; Reston and McDermott 2011), the rifting of the SCS was inherently influenced by the composition and the stress field from different continents nearby, such as the Indian Peninsula, the Pacific, and the Indo-Australian Plate. However, previous works have proved the detachment systems found in the margins of the SCS are common features of the north Atlantic rift margins (Péron-Pinvidic and Manatschal 2009;

Electronic supplementary material The online version of this article (doi:10.1007/s11001-016-9295-y) contains supplementary material, which is available to authorized users.

✉ Chuanchuan Lü
clu@mail.iggcas.ac.cn

¹ Key Lab of Petroleum Resources Research, Institute of Geology and Geophysics, Chinese Academy of Sciences, Beijing, China

² Department of Geology and Geophysics, Woods Hole Oceanographic Institution, Woods Hole, MA, USA

³ Key Lab of Marginal Sea Geology, South China Sea Institute of Oceanology, Chinese Academy of Sciences, Guangzhou, China

Reston and McDermott 2011; Ding et al. 2013; Franke et al. 2014).

Various models have been proposed to explain the processes of the crustal extension of deep passive margins, and how the oceanic crust accreted from the breakup of the continental margins, the detachment model is generally accepted (Wernicke 1981; Lister et al. 1986; Boillot et al. 1987; Péron-Pinvidic and Manatschal 2009). The detachment system typically results in asymmetric rift margins, which are often characterized by one side containing a wide-rift and hyper-extended continental crust, and the conjugated part possessing a relatively more abrupt crustal thinning and narrower transition zone. Extension discrepancy has been observed between the whole crust and the upper crust on both conjugate margins (Reston 2007). The whole crustal stretching estimation derived from geophysical modeling and the upper crust stretching from normal faults by seismic method (Chen 2014). Based on the extensive work on the Iberian and Newfoundland conjugate margins (Whitmarsh et al. 2001; Tucholke et al. 2007; White and Smith 2009), the depth-dependent stretching model involved with decoupling the upper brittle and lower ductile crust has been used to explain this discrepancy in the SCS (Ding et al. 2013). Another explanation is that the polyphase extension event or subseismic faulting may exaggerate the inconsistency (Reston 2007; Reston and McDermott 2014).

In this study, we focused on the geological interpretation of the structure from a deep seismic transect (Fig. 1) across the northern margin of the southwest subbasin (SWSB), where a polyphase faulting occurred prior to seafloor spreading. Based on combined analysis of the multi-channel seismic interpretation and wide-angle seismic tomography of the seismic transect, we provided evidence from pairs of rifted margins to compare the variation of crustal thinning and the time of syn-rift infill and the domain of the continent-ocean transition, which helped us to uncover the evolutionary pattern of the margin of the SWSB. It allowed us to examine the manner in which deep detachment faults and rigid blocks impact the final lithosphere breakup, on which we discuss the temporal and spatial rift development of the SWSB margin.

Geological setting

The SWSB is one of the three oceanic basins located in the SCS. It is located between the Xisha Islands (Paracel Islands) and the Nansha Islands (Spratly Islands), and is surrounded by several rigid blocks, including the Macclesfield Bank, Zhongjian Massif, Reed Bank and Zhenghe Massif. Its southwestern tip indicates features of a failed rift (Li et al. 2012b) where its fossil spreading center diminished, to the

east it is bounded by the Zhongnan fault zone that separates it from the eastern subbasin. The SWSB formed ~ 23.6 to ~ 16 Ma in the Cenozoic following a spreading ridge jump (Briais et al. 1993; Barckhausen and Roeser 2004; Li et al. 2014).

Prior to the seafloor spreading, the dominated tectonic environment of the continental margins of SWSB experienced changes from Andean-type convergent setting to episodic extension and erosion setting during the era from the middle Mesozoic to late Cenozoic (Taylor and Hayes 1983; Ru and Pigott 1986; Hall 2002; Shi et al. 2005). The earliest extension of the Cenozoic started from the northern margins of the SCS in the Paleocene (Ru and Pigott 1986), where the Xisha Through locates and works as a failed continent breakup in the northwestern margin (Schlüter et al. 1996; Qiu et al. 2001). As the extension gradually propagated to southwest (Li and Song 2012; Ding et al. 2013; Franke et al. 2014), several episodes of extension occurred in the margins of the SCS. From the seismic profile, the two main episodes of rifting in the SCS were observed around nearly all the offshore the Cenozoic basins (Cullen et al. 2010), which date from the early Paleocene to Eocene and late Eocene to early Miocene. In the continental margins of the SWSB, a highly attenuated crust and an ultra-wide rift half graben/half host structure was the result of progressive stretching with additional regional extension events occurring along different segments of the rift grabens and basins from the late Eocene to the middle Oligocene (Savva et al. 2014). After the Dangerous Grounds had collided with Borneo in the middle Miocene (Hutchison 2004; Clift et al. 2008; Cullen et al. 2010; Hutchison and Vijayan 2010), the stress dominant setting of the southern margin changed into a compression. There are several basement high features around the SWSB, including the Macclesfield Bank, Reed Bank, Zhongjian Massif and Zhenghe Massif. Their Precambrian metamorphic basements (Yan and Liu 2004) suggested that they deformed little and remained as rigid blocks during the progressive continental lithosphere rifting, and have a continental origin from the South China Block (Yan et al. 2014). They acted as a sharpener during the breakup of the continent until the advent of seafloor spreading of the SWSB (Ding and Li 2016).

Experiment

Data acquisition

This 880-km-long ocean bottom seismometer (OBS) transect across the SWSB from the Xisha (Paracel) Islands region to the Nansha (Spratly) Islands is comprised of two profiles. We collected the data separately in April 2009

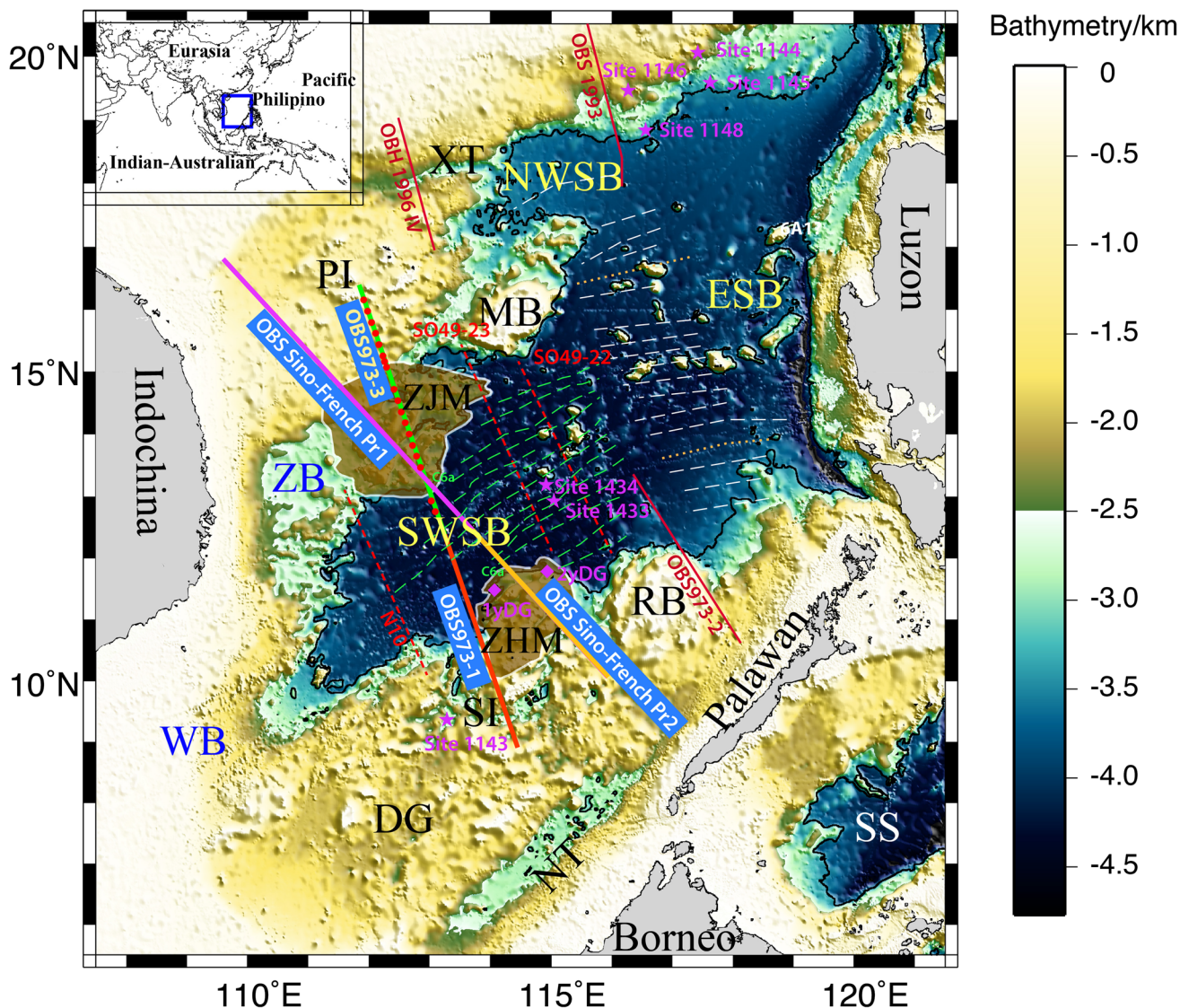


Fig. 1 Location of the study region and the previous deep seismic profiles. One iso-bath shown on the maps is 3500 m, which outlines the continental oceanic boundary of the SCS approximately. White to yellow corresponds to the continental shelf and upper slope, respectively. Oceanic sub-basins are marked with yellow letters: SWSB southwest subbasin; NWSB northwest subbasin; ESB east subbasin. Offshore Cenozoic sedimentary basins are marked with blue letters: WB Wan’an Basin (Nam Con Son Basin); ZB ZhongJianNan Basin (Phu Khanh Basin). Green and white dash lines sketch the negative magnetic anomalies (Li et al. 2014) in different oceanic sub-basins of the SCS. Green solid lines show the location of the OBS973-3 with coincident MCS/OBS data conducted in 2011,

and the pink and orange solid lines (OBS Sino-French Pr1 and Pr2) are two OBS profiles acquired by Sino-French collaboration in 2011. The red dots along green line indicate the position of OBSs. Other OBS profiles are shown using red lines (OBS973-1, OBS973-2, OBH 1996IV, OBS1993). Red dash lines indicate the previous MCS profiles in the SWSB (Li et al. 2012b). Purple stars and diamonds indicate the location of International Ocean Drill Programs (IODP 184 and IODP 349) drill sites and dredged sites. XT Xisha Through; NT Nansha Trough (Northwestern Borneo Trough); MB Macclesfield Bank (Zhongsha Islands); RB Reed Bank; ZM Zhenghe Massif; PI Paracel Islands (Xisha Block); SI Spratly Islands (Nansha Block); DG Dangerous Grounds; SS Sulu Sea

(OBS973-1, the southern part) and March 2011 (OBS973-3, the northern part) via the two legs of “Project 973 Cruise” to study the margins of the SWSB. The two OBS profiles were both conducted by the R/V SHIYAN 2 of the South China Sea Institute of Oceanology, Chinese Academy of Sciences. An array of four large volume bolt airguns with a total volume of 6000 cubic inches comprised

the seismic source and fired at 300 m spacing at a depth of 10 m. In total, 20 OBSs were deployed along the profile of OBS973-3 every 20 km, and 10 of them were single sphere OBSs equipped with 3-components 4.5 Hz “SEDIS-V” geophones and one hydrophone, manufactured by GeoPro (Germany). The other OBSs were equipped with 3-components 60 s⁻¹ geophones and one hydrophone (Institute of

Geology and Geophysics, Chinese Academy of Sciences). On average, one in 20 OBSs were not recovered, and an additional OBS has troublesome data but was recovered recently (Wang et al. 2016). A single channel seismic profile along the OBS profiles by R/V SHIYAN 2 was employed to simultaneously acquire additional bathymetry and sediment thickness data.

Accordingly, the multi-channel seismic (MCS) data were acquired along the profiles by M/V TANBAO of the Guangzhou Marine Geological Survey. Its airgun array has a capacity of 5080 cubic inches towed at a depth of 9 m, and a 480 channel streamer recorded at a sample rate of 2 milliseconds (ms) at a depth of 10 m. Shots were fired at every 37.5 m and recorded on the streamer at an interval of 12.5 m.

MCS data interpretation

The MCS data of OBS973-1 (NH973-1) have been processed and interpreted previously (Zhao et al. 2011; Ding et al. 2013, 2015; Song and Li 2015; Ding and Li 2016). Therefore, we were able to use many previous results as references to process the MCS data of OBS973-3 through incorporation a similar workflow, including normal move-out correction, stacking, band-pass filtering, predicted deconvolution, multiple attenuations in the frequency-wavenumber domain and multiples attenuations using Radon transform. The data set was then migrated using pre-stack time migration. The specific processing technique and part of the resulting image were published in another paper (Sun et al. 2011).

In light of the drill sites 1433/1434 from the IODP Expedition 349 (Li et al. 2015b), the MCS data interpretation was performed by referring to several adjacent MCS profiles (R1, R2, R3, R4 from the Guangzhou Marine Geological Survey as shown in Fig. 2), including the seismic profiles in the oceanic basin (Li et al. 2012a; Ding and Li 2015) and the southern margin (Ding and Li 2011; Yao et al. 2012; Lü et al. 2013; Franke 2013; Ding and Li 2015; Song and Li 2015). To interpret our time migrated profiles ‘OBS973-3’ and ‘OBS973-1’, we performed the seismic sequence stratigraphy analysis using the GeoFrame package (Schlumberger) to categorize the seismic strata of Cenozoic stratigraphy into five major tectonostratigraphic units. Our interpretation used four major unconformities, corresponding to the tectonic events from the first rifting to the breakup of the continental margin. We identified five different units along our seismic transect between Zhongjian Massif and Zhenghe Massif, namely the post-rift unit, the late syn-rift unit, the eastern rift unit, the early syn-rift unit and the init-rift unit. Considering the significant events during the rifting stages of the SCS, the units were separated by the horizons T50, T60, T70, T80 and Tg along

‘OBS973-3’ (Fig. 3a, b) and ‘OBS973-1’ (in supplementary figure).

The two most prominent unconformities, namely the breakup unconformity (BU, as shown by horizon T50 using a cyan line in Fig. 3) and the rift-onset unconformity (ROU, as shown by the black line in Fig. 3a, b), define the syn-rift units. Both are believed to be diachronous due to the overall southwestward propagation of rifting-drifting in the SCS (Briais et al. 1993; Li et al. 2014). Their diachronism along the margins has been addressed previously by several papers (Hutchison and Vijayan 2010; Franke et al. 2011; Ding et al. 2013; Steuer et al. 2014; Song and Li 2015; Morley 2016). Furthermore, as previous papers have discussed, the BU often joins with another unconformity, namely the middle Miocene unconformity, which is often found in the post-rift unit caused by subsidence following the cessation of seafloor spreading (Cullen et al. 2010; Ding et al. 2013; Song and Li 2015). In our paper, we focused on the rifting evolution of the continental margins of the SWSB, thus the strata above the seismic sequence BU were treated as one unit.

The timing of rift initiation varies from region to region, though extensive seismic profiles and drilling wells have been conducted in the SCS. As shown in a review of the major unconformities in the SCS (Morley 2016), a significant inconsistency in the seismic sequence interpretation exists in both the northern and southern margins. Concerning the nearby results from the Zhongjiannan Basin and Reed Bank, respectively (Chen and Zhong 2008; Yao et al. 2012), we interpreted the timing of ROU (Tg) of the profile ‘OBS973-3’ in the Zhongjian Massif as Late Eocene (~55 Ma), while the ROU of the profile ‘OBS973-1’ in the Zhenghe Massif as Early Paleocene (~65 Ma).

The horizon T80 is a regional unconformity distributed in the half graben/half host in the Zhenghe Massif of the southern margin. It resulted from the tectonic subsidence of the Xiwei movement (~38 Ma) in the SCS, but also corresponds to the Sarawak movement in the southern margin (Hutchison 2004; Yao et al. 2012).

The horizon T70 is parallel to the horizon of T80 in general and represents the lithosphere breakup of the eastern SCS (according to the IODP 349 site U1345). Corresponding to the so-called ‘SCS movement’ in the Late Oligocene–Miocene (~31 Ma) in NE Palawan, it can be traced in most of the Cenozoic Basin of the SCS, which suggests either an inter-rift status of the continent margins, or that the rising asthenosphere enabled the uplift of the margin in the SCS (Falvey and Mutter 1981).

The horizon T60 represents the kinematic phase shifts of the SCS rift as a result of the rifting rotation beginning from a N175° direction towards a N165° direction (Sibuet et al. 2016). This is closely followed by the spreading

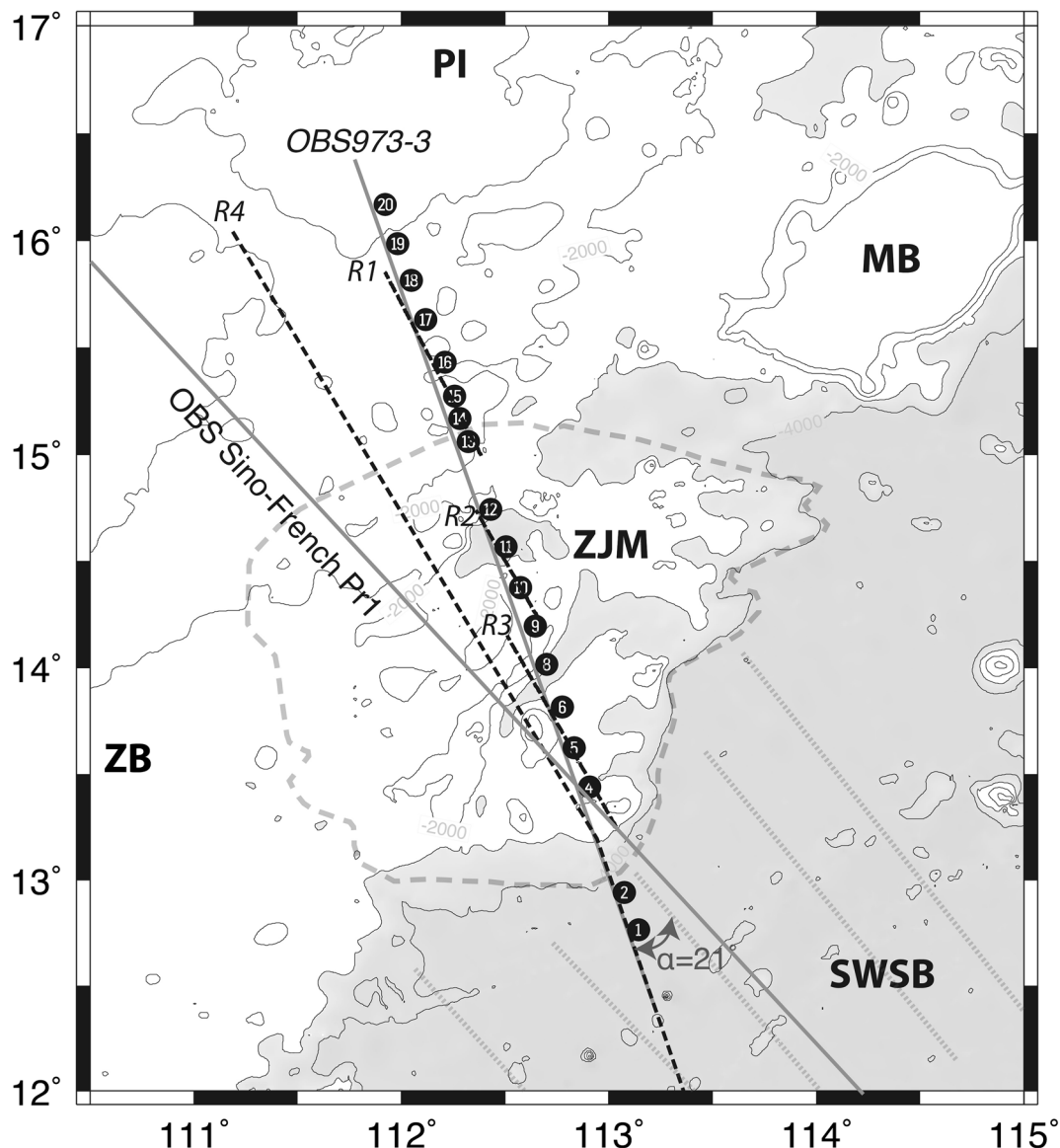


Fig. 2 The seismic data set of OBS973-3 on the northwestern margin of the SWSB. The MCS interpretation of OBS973-3 referred to several adjacent MCS profiles (profiles R1, R2, R3, R4 shown with *dash lines*). The encircled numbers are the OBSs with usable data and the *solid gray line* are coincident MCS profile along OBS973-3.

Another OBS profile in the thin *solid black line* “OBS Sino-French 2011 Pr1” was also conducted in 2011 but without acquiring the MCS data. SWSB southwest sub-basin; MB Macclesfield Bank (Zhongsha Islands); PI Paracel (Xisha) Islands; ZB, ZhongJianNan Basin (Phu Khanh Basin)

ridge-jump event around 23.6 Ma in the Eastern SCS (Li et al. 2014). With the bumpy spreading rate from 70 mm/yr to 30 mm/yr and the dominant faults trending from E–W to NE–SW (Savva et al. 2014), a series dextral strike-slip fracture zone formed (Steuer et al. 2014) resulting in a weakening of the rigid blocks. The ‘late synrift unit’ signifies the abrupt changes in the depositional environment and sedimentary input during the last 3.5 million years.

The horizon T50 marks a sharp transition from extension to thermal subsidence where the cessation of the

continental crust rifting occurred and formed the breakup unconformity (BU). Between the Zhongjian Massif and Zhenghe Massif, where the magnetic chrons C6a and C6b (~22.5 Ma) are located nearby, the ages of the BU can be estimated. It represents the beginning of the regional subsidence associated with lithosphere cooling around those rigid blocks. As it is characterized by intense erosion and deformation, it often joined with the horizon T40 (Middle Miocene Unconformity) (Hutchison and Vijayan 2010; Song and Li 2015). This represents the cessation of seafloor

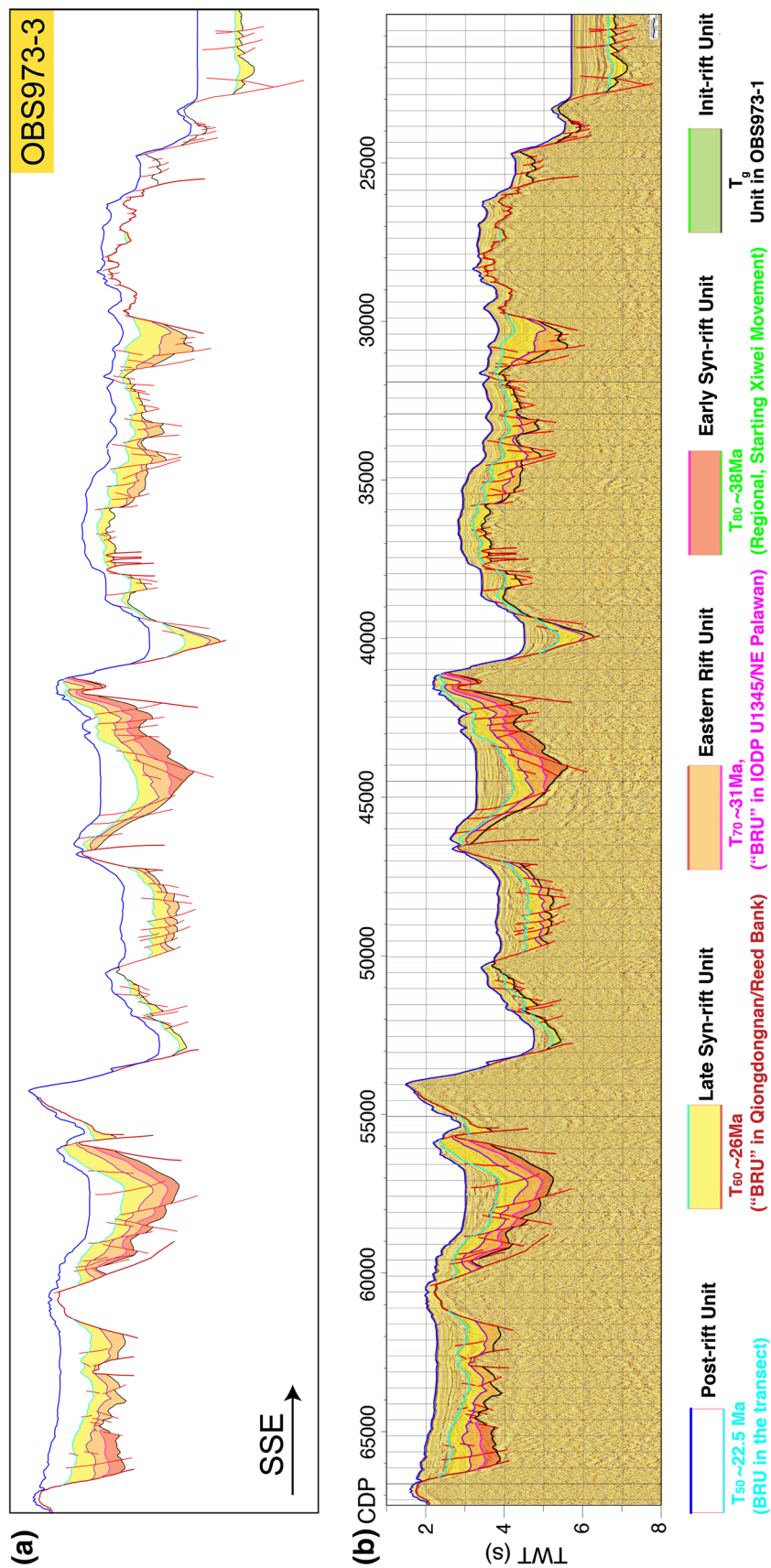


Fig. 3 The interpreted result of the MCS data of the OBS973-3 superimposed on the time migrated seismic image (a, b). The seafloor and acoustic basement are shown in *blue* and *black* *solid lines*, and the fault lines are shown with *red lines*. The sedimentary layers between *blue* and *green horizons* represent the subsidence unit after the seafloor spreading ceased, and the *black* sedimentary layers filled with *yellow* correspond to the subsidence during seafloor spreading. The sedimentary layers filled with *orange*, *red* and *green* represent the two stages of syn-rift and pre-rift subsidence, respectively

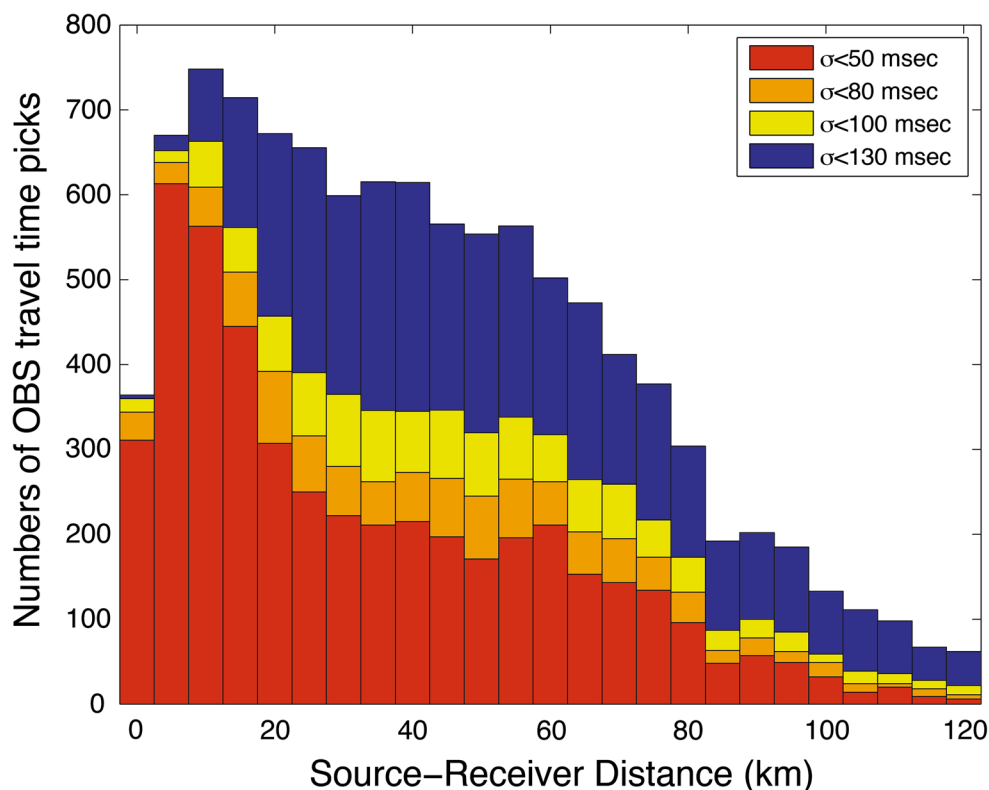


Fig. 4 Histograms indicate the travelt ime uncertainty of all OBS phases by distribution of source receiver offsets. The range distribution is shown for travelt ime picks within error bounds

spreading and shows strong diachronism as a result of the southwestward propagation of seafloor spreading (Li et al. 2012b), though it corresponds to a single period event.

In summary, our SCS interpretation indicated a slightly different rifting history across the conjugate margins of the SWSB during the Early Eocene to Late Oligocene period. Relatively earlier sedimentary units (init-rift unit) indicate that the southern margin of the SWSB experienced at least one more tectonic movement than its conjugate part. Furthermore, a relatively thicker post-rift unit also reveals that it has been affected by increased tectonic subsidence following the continental breakup in comparison to the north, such as the Danger Ground in the southern margin colliding with NW Borneo, suggesting that the dominant tectonic configuration changed from extension to compression during the later stages of the Miocene.

OBS data processing

The reflection and refraction data of the OBSs was handled using time correction, station relocation, band pass filtering (3–15 Hz), predicted deconvolution and seismic amplitude compensation. Through picking the travelt ime of direct waves from the common receiver gathers from OBS data,

we calculated the accurate locations of the OBSs on the seafloor using linear damping inversion. As for the precise shot time of the airgun arrays, we utilized a specialized seismometer located on the ship deck to record the airgun triggering time, and then cross-referenced this with the timer of the airgun controller system. The timing errors between the two systems were smaller than 10 ms.

We processed data from 18 OBSs and obtained 5715 travelt ime picks in total, consisting of 2928 turning waves (Pg) traveling in the crust and 2670 Moho reflections (PmP). All the travelt ime and their uncertainties were chosen visually in the OBS common receiver gathers. We recorded Pg arrivals to distances of 20–65 km on all the OBSs, and also recorded PcP and PmP arrivals reflected in the crust and on the Moho gathers. The travel-t ime uncertainties (σ) were calculated based on the signal-to-noise ratio calculated as the square root of the ratio between the maximum trace amplitudes in a 250-ms window before and after picking (Zelt and Forsyth 1994). The uncertainty of the crustal arrivals is clearly much higher if the interpreted arrivals have a relatively larger offset (as the statistic indicates in Fig. 4). At larger offsets, we picked fewer due to the unambiguity of the lower signal to noise ratio. Travelt ime picks were most observed within the range of source-receiver offsets, at 5–50 km. The common receiver gathers from OBS#pos05

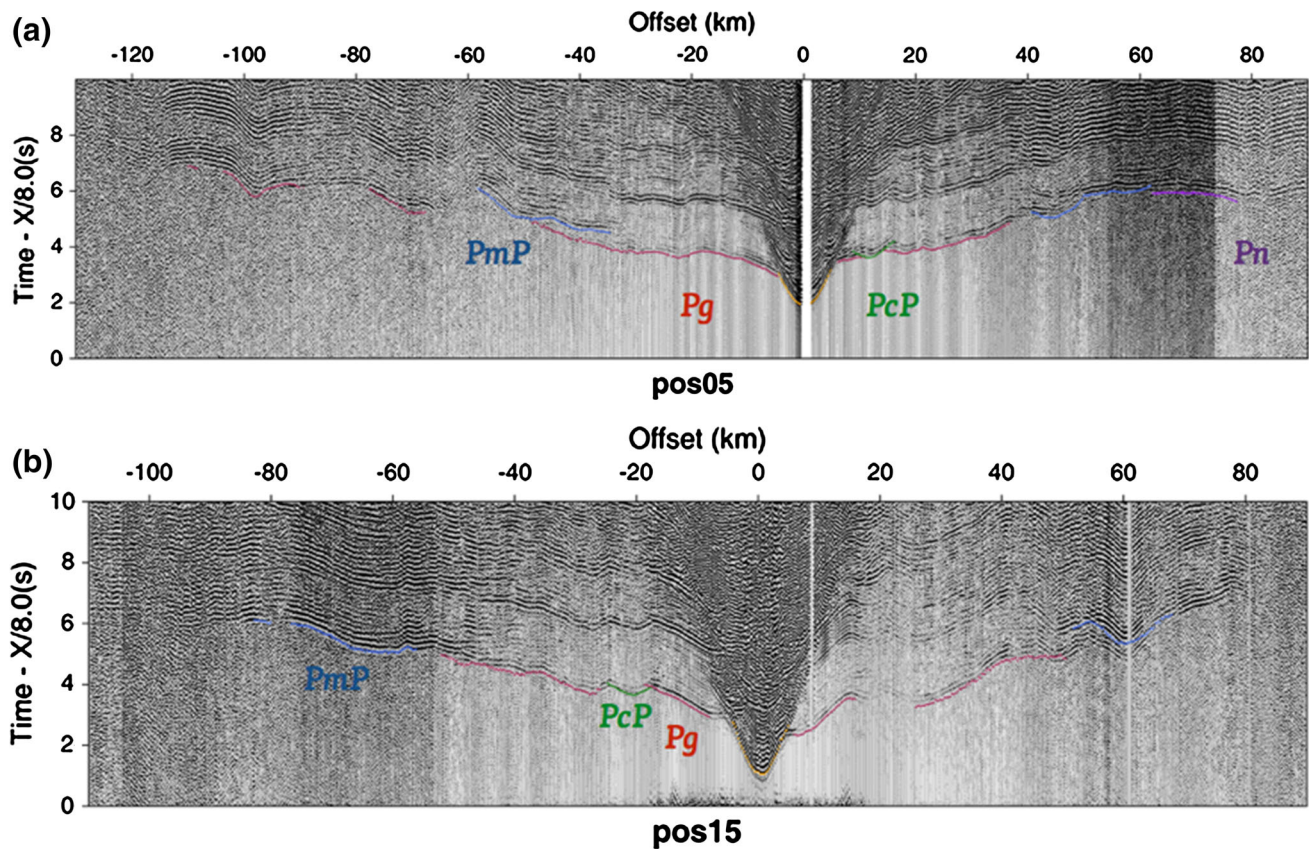


Fig. 5 Examples of the OBSs data of OBS973-3 (the other OBS results are in the supplementary material). Vertical record of OBS#pos05 and OBS#pos15 superimposed with computed traveltime. The vertical axis (time) is reduced by 8.0 km s^{-1} and represents the traveltime of P wave in seconds. The horizontal axis is the model offset in kilometers. The Pg phases are shown in red and represent the

turning wave in the crust. The PcP phases are shown in green and indicate the reflected wave within the crust. The PmP phases are shown in blue and indicate the reflected wave from the seismic Moho. The Pn phases are shown in purple and represent the head wave along the seismic Moho (not employed in the inversion)

and OBS#pos15 are shown as examples in the Fig. 5, and the rest of the OBSs are shown in the supplementary material.

Seismic modeling procedures

Seismic tomography strategy

Due to the consistency of the temperature ($2.4\text{--}4 \text{ }^\circ\text{C}$) and salinity (34.6) in the deep water of the SCS across all seasons (data provided by the China Oceanic Information Center), the seawater velocity was consistently set to 1.49 km s^{-1} in our model. The seafloor depth along the transect is given by a single channel seismic data. The sediment layers were split into three layers for wide-angle seismic modeling at most, based on the interpreted result of coincidence MCS data. The velocities varied from 1.6 to 2.4 km s^{-1} (sediments after the late Oligocene), $2.5\text{--}2.9 \text{ km s}^{-1}$ (sediments between the Oligocene and late Eocene), and $3.0\text{--}3.9 \text{ km s}^{-1}$ (sediments before the late Eocene). The continental sediment depth was constructed

from coincidence MCS data using the time-to-depth conversion formula, which was calculated from the stacked section of the MCS data of the Guangzhou Marine Geological Survey (Wang et al. 2006b; Yao et al. 2012).

$$z = 254.38t^2 + 786.86t + 8.76 \quad (1)$$

Furthermore, the oceanic sediment depth was constructed from the IODP Expedition 349 site U1433/U1434 where a complete suite of logging samples from the seafloor to the oceanic basalt was obtained (Li et al. 2015a).

$$z = 0.000152626t^2 + 0.714658t \quad (2)$$

where z is the depth of the sediment layer in meters and t is two-way traveltime from the bottom of the seafloor in milliseconds. We constructed the initial velocity model after employing the MCS interpretation results, and then used the inversion method of JIVE3D (Hobro et al. 2003) to obtain a P-wave velocity model of the northern margin of the SWSB.

The inversion package of JIVE3D is a regularized joint refraction and reflection traveltime tomography inversion,

Table 1 Traveltime residuals and Chi squared error for all the phases by the wide-angle seismic tomography

Seismic phase	Number of picks	Chi squared χ^2	Traveltime residual RMS
Refraction in the crust (Pg)	2928	1.579	0.126
Internal crust reflection (PcP)	117	1.97	0.493
Seismic Moho reflection (PmP)	2670	1.361	0.106
All phases	5715	1.485	0.124

which simultaneously solves for the seismic velocity structure and reflecting interface such as ‘the seismic Moho’ and internal crustal reflectors. To integrate with the previous MCS interpretation result, we chose to exclude the sedimentary layers velocity inversion. Instead, we only used phases, such as Pg, PmP and PcP, to obtain the crustal velocity structure, including the seismic Moho and “floating” reflectors within the crust, such as faults or fracture zones.

Though the inverse problem of the JIVE3D package employed an iterative “jumping” strategy to diminish the initial model effect (Shaw and Orcutt 1985), we divided the crust into two layers to constrain the upper and lower crusts with different velocity gradients. The velocity model is parameterized as a 2D 470 km-by-25 km mesh with a constant horizontal nodal spacing of 1 km and a variable vertical nodal spacing from 0.5 to 1 km at the upper and the lower crust. Since we did not employ the Pn phases that are rarely picked from the profile, we applied a velocity of 8.0 km s^{-1} in the shallow upper mantle and used the long-offset Pg and the PmP phases to obtain the undulation of the seismic Moho. The initial velocity of the crustal model was set up linearly but with a different gradient from 4.0 km s^{-1} below the seafloor to 7.8 km s^{-1} at the crust-mantle boundary. The process of the inversion requires several parameters to setup the smoothing levels of the preferred velocity structure and its gradient. Here we chose more horizontal velocity weighting than the vertical weighting as our configuration of the OBSs is at 20 km spacing, and then set up the inversion scheme for the velocity gradient including a changing gradient for the upper crust and a constant gradient for the lower crust.

Inversion velocity structure

The result of the inversion was chosen based on the model with the lowest traveltime residual root mean square (RMS) and best χ^2 (Zelt et al. 2003), as the 20 km-spaced OBS profile cannot solve the model perfectly even if the MCS results are used as constraints. The formal error analysis for individual phases is summarized in Table 1. The final model is well constrained with a total RMS misfit of 124 ms between the calculated and picked traveltime, and the normalized χ^2 is around 1.5.

To better interpret our crustal velocity model, we removed the velocity isocontours from the sedimentary and mantle layers from Fig. 6 since they were not involved in our inversion. Our model is inverted sequentially from the upper to the lower crust layer using the travel time from the near-offset Pg and the far-offset Pg. The velocity cells lacking any coverage of the model were blanked by a gray shadow, and the interfaces without any reflection (PmP and PcP) were erased from the crust-mantle interface and internal crustal reflectors.

Between the acoustic basement and the velocity isocontour of 5.5 km s^{-1} , strong velocity variation ranging from 4.0 to 5.5 km s^{-1} revealed rather sharp horizontal changes at the topmost crust, though the gradient maintained small perturbations with an associated wavelength bracketed between 40 and 60 km, such as the part between offset 90 and 150 km or 320 and 360 km in our model. This low-velocity layer below the basement conflicts with the continental crust velocity obtained from the global extension crustal model ‘CRUST 5.1’ (Mooney et al. 1998), in which the velocity starts around 5.5 km s^{-1} from the uppermost crust. However, considering the apparent low velocity (4.0 – 5.5 km s^{-1}) of Pg that we observed in our OBS data, considering the station OBS#pos08 and OBS#pos12 as examples (Fig. 7), located directly on the basement slope without any sediment (see Fig. 6 for their location, Fig. 3 for their sediment structure and the supplementary material for all better resolution OBS images), we believe those are neither the artifacts relating to the over-estimated velocity modeling of the sedimentary layers, since there are no sediments nearby (zones highlighted in orange in Fig. 7), nor poorly resolved inversion since we obtained a resolution test of 40 km by 4 km in horizontal and vertical length (in “Inversion velocity structure” section). Additionally, a similar phenomenon has been identified in the study of another adjacent OBS profile ‘OBS Sino-French 2011 Pr1’, which showed a similar pattern of low-velocity isocontours ranging between 4.0 and 5.5 km s^{-1} in a similar spatial wavelength (Pichot et al. 2014), as well as the OBS profile ‘OBS973-1’ in the southern margin of SWSB (refer to Fig. 1 for its location), which was modeled using a different strategy (Qiu et al. 2011) where the velocity isocontour 4.0 km s^{-1} was used to define its basement boundary. Comparing our tomography model with the chronostratigraphy result from our

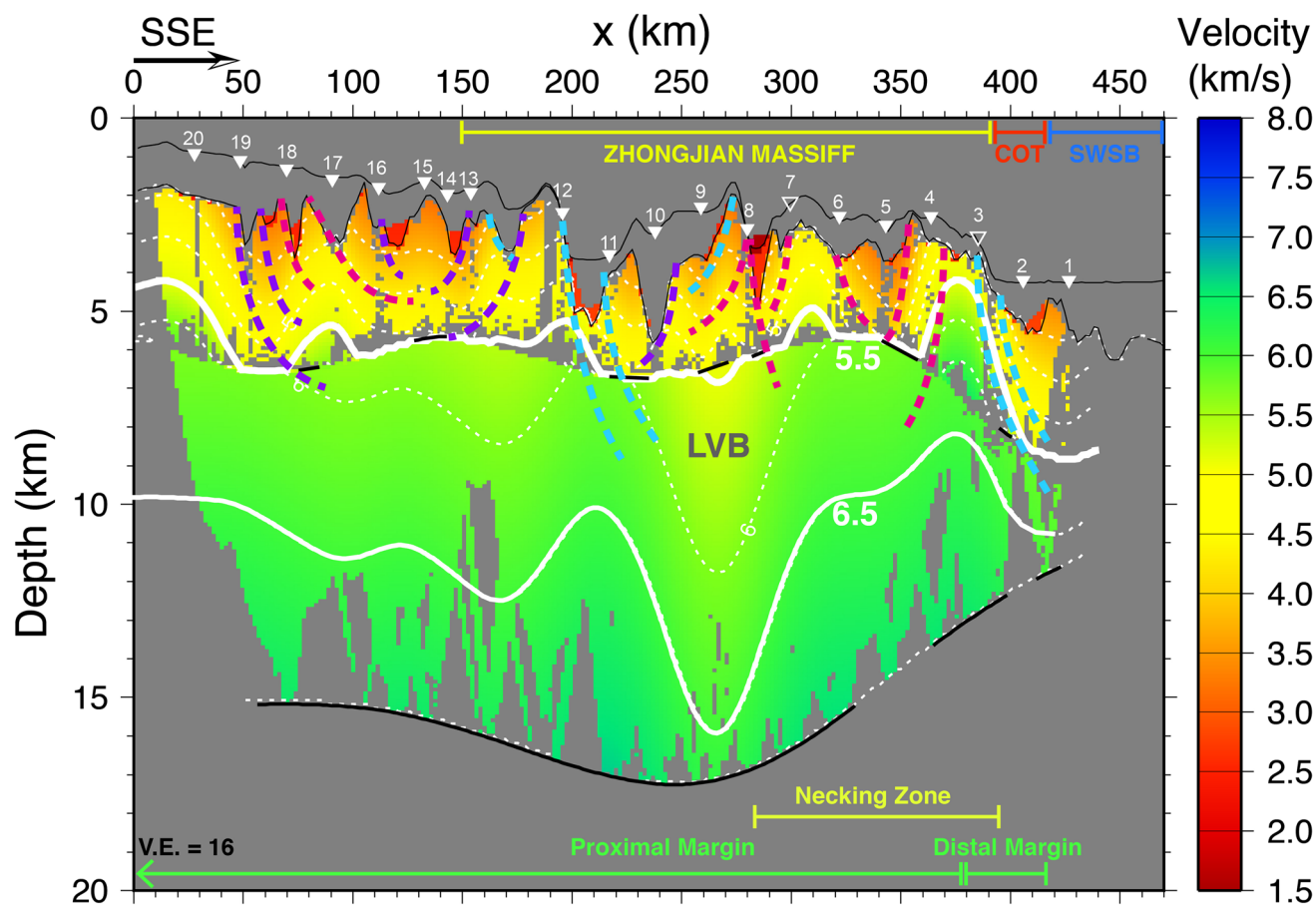


Fig. 6 Optimal P-wave velocity model of the OBS profile ‘OBS973-3’ with our interpretation and the vertical exaggeration of 16. The seafloor and the acoustic basement shown in thin black lines are derived from the MCS data. Heavy black solid lines are the seismic Moho and inner crustal reflectors, which are inverted from the PmP and PcP phases. The thin white dash lines are the velocity isocontours drawn every 0.5 km s^{-1} , and the thick white dash lines represent the

velocity isocontours 5.5 and 6.5 km s^{-1} which represent the décollement plane and the boundary between upper crust and lower crust, respectively. The purple, red and cyan dash lines represent successive phases of crosscutting faults. The gray shadow zones represent the areas without any ray coverage. The filled and unfilled triangles represent the OBSs with or without useful data

coincident MCS interpretation (Fig. 3), we estimated the velocity isocontours between 4.0 and 5.5 km s^{-1} may not represent a typical stretched continental crust, but rather an upper fracture layer (hereafter UFL) caused by more than one phase of faulting under a series of extensional events. We also observed the sharp horizontal changes in velocity from the location of OBS#pos04 to OBS#pos02, which may represent the detachment fault system during the final breakup of the continental lithosphere (Ding et al. 2013; Franke et al. 2014). Thus, the velocity isocontour of 5.5 km s^{-1} roughly corresponds to the décollement plane that separates a complex UFL above with the normal continental crust, and the inner crustal reflectors were imaged as several low-angle basal fault planes (shown in the upper crust in Fig. 6). Since the morphology of the UFL corresponds well with horst-and-graben fabric in the sedimentary layer, upon consideration of the different periods of subsidence and the depth of the normal faults

slip, we deduced the relationship between the UFL and the rifting period of the continental margin of the SWSB by adding different phases of basal fault to interpret our velocity model (Fig. 7).

Another remarkable phenomenon is the variation in sharp lateral velocity occurring under the UFL at the depth from 6 to 14 km below sea level, which locates between OBS#pos07 and OBS#pos12 in our final model and coincides with the extent of a rigid tectonic block, the Zhongjian Massif. Compared with the global crust, its vertical continental gradient has been significantly reduced, and it stands out as a low-velocity body (hereafter LVB) in the upper-middle crust below the center of ZJM. We took the velocity isocontour 6.5 km s^{-1} as the boundary between the upper and lower crust (the lower thick white line as shown in Fig. 7) since it usually separates the brittle layer and ductile layer within continental crust under an extensional setting (Christensen and Mooney 1995).

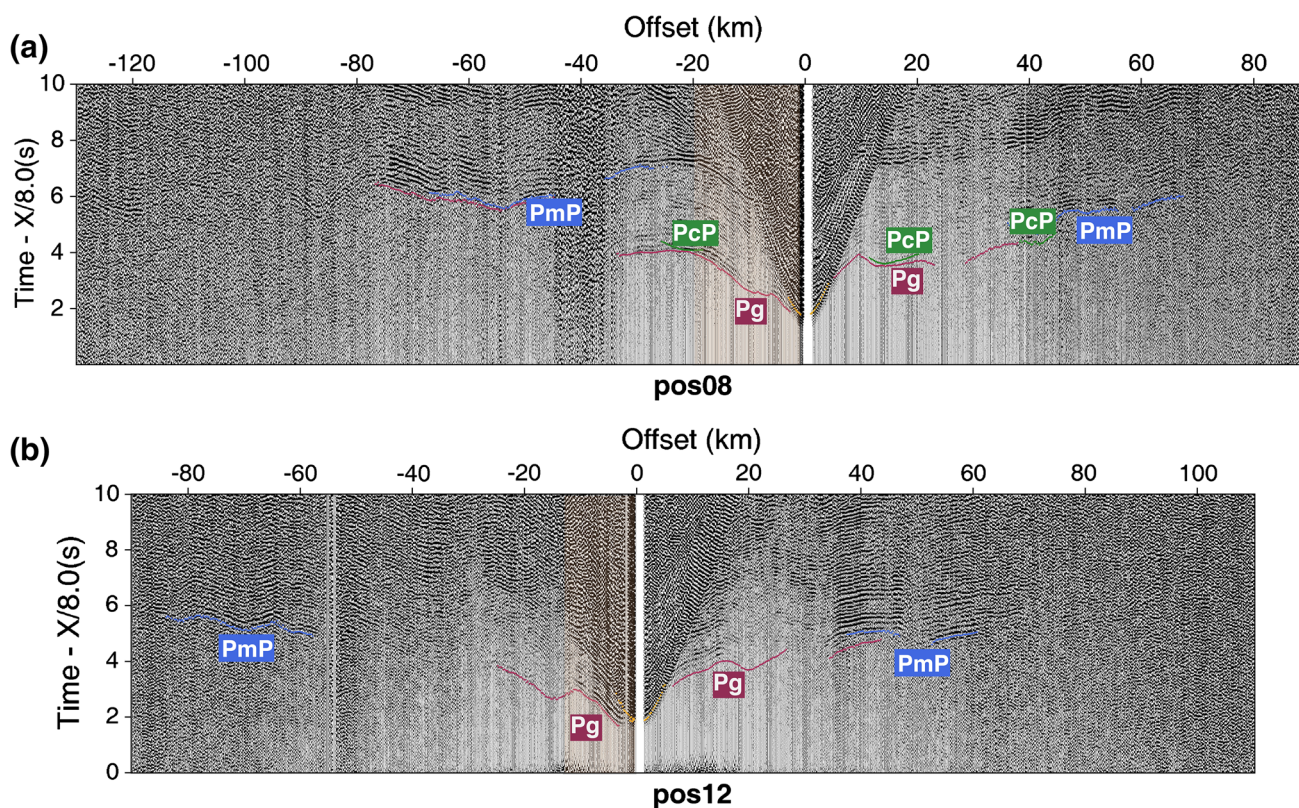


Fig. 7 Example of two OBSs data located directly on the acoustic basement in the OBS973-3. The location of the OBS#pos08 and OBS#pos12 can be found in Figs. 2 and 6. The LVBs' apparent velocity is easily spotted within the orange shaded area. The vertical record of OBS#pos08 and OBS#pos15 is superimposed with the computed traveltime. The vertical axis (time) is reduced by

8.0 km s^{-1} and represents the traveltime of P wave in seconds. The horizontal axis is the model offset in kilometers. The Pg phases are shown in red and indicate the turning wave in the crust. The PcP phases are shown in green and indicate the reflected wave within the crust. The PmP phases are shown in blue, and represent the reflected wave from the seismic Moho

The thickness of the LVB can be measured from velocity isocontours $5.5\text{--}6.5 \text{ km s}^{-1}$, and it is 1 km thinner compared with the LVBs observed from other OBS profiles that are located across the rigid blocks in the continental margins of SCS, such as Zhongjian Massif, Zhenghe Massif and Reed Bank. The maximum thickness of LVBs from 'OBS Sino-French Pr1' and 'OBS Sino-French Pr2' is 10 km, while 11 km from 'OBS973-2' (Pichot et al. 2014; Niu et al. 2014).

The low crustal layer, ranging from 6.5 to 6.9 km s^{-1} , shows a consistent thickness of 5 km except for the part below the LVB from offset 200 to 300 km in our model. The offset 200 km, where OBS#pos12 located, corresponds to ~ 2000 km water depth, which marks the transition zone from the continental slope and continental rise. From offset 360 to 260 km, the lower crust thickness varies from 5.0 to 4.5 km and drops sharply to nearly 1 km at the offset 130 km and then returns to 5.0 km. Therefore, we speculate that the thickness of lower crust barely changed during the sequence of rifting events if the existence of the rigid block, the LVB, is not considered. On the contrary, the slope of the seismic Moho varies considerably on either side of the LVB.

The Moho depth at the northern side changes slightly from 15.2 to 17 km, while it rises from 17.2 to 11.5 km at the necking zone, resulting in a dip of 2.1° .

In summary, our velocity model in the northern margin of the SWSB indicates strong variation in lateral velocity within the upper crust and a relatively homogenous lower crust. The LVB at the intermediate depth of the upper crust denotes the existence of a rigid block. Moreover, there was no high-velocity body imaged within the crust. The Moho undulation remains mostly unchanged until the end of the proximal margin that marks the start of the necking zone.

Tomography result assessment

The forward problem of JIVE3D is solved based on the ray perturbation theory rather other than numerical methods; thus to assess the resolution we performed the standard check-board test (Zelt 1999). The resolution test indicated that a $40 \text{ km} \times 4 \text{ km}$ resolution can be achieved in our 20 km-spaced OBSs configuration (Fig. 8a, b). We constructed our synthetic test model using the same mesh as the final model and with $\pm 5\%$ sinusoidal perturbation anomaly (shown in

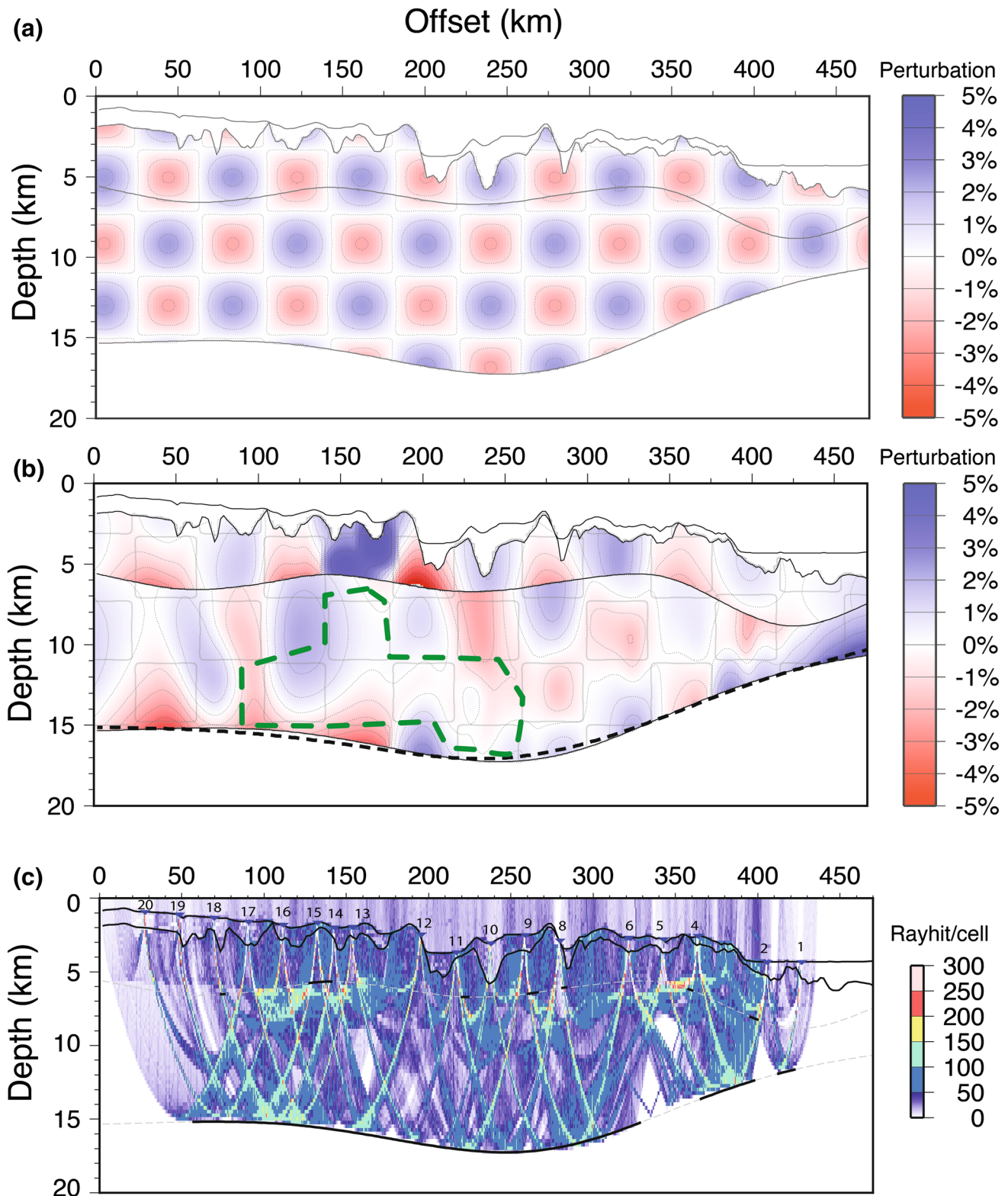


Fig. 8 The checkerboard resolution test and its ray coverage density, with a vertical exaggeration of 10. **a** The initial checkerboard velocity perturbation model, the size of the anomalies is in the dimension of 40 km by 4 km indicated by *thin grid lines*. **b** The reconstructed checkerboard resolution model. Synthetic model velocity contour was superimposed by *gray square* and the reconstructed velocity anomaly

and the recovered Moho was shown by color cell and the *black dash lines*. Our non-satisfactory resolution was encircled by a *green dash line*. **c** The density of the refracted and reflected rays travelling in final velocity structure layers. The ray density is counted by the dimension of 1 km along the distance and 0.5 km along the depth. The OBSs are denoted by 18 inverted triangles

Fig. 8b). The synthetic refraction and reflection traveling time were calculated from the synthetic model, which combined the perturbation anomaly with the linear velocity gradient model. Using the same shot-receiver configuration as the observed data, we calculated the inversion and reconstructed velocity anomalies (shown in Fig. 8b).

The checkboard result indicates a satisfactory recovery in the upper crust and part of the lower crust, drawn excluding the zone encircled by the green dash line (Fig. 8a, b). Our tomographic inversion may overestimate the amplitude of the anomalies within the part of the upper crust as the density of the ray converges of the model are not even (Fig. 8c). Furthermore, the reconstructed result suggested that it was insensible to the undulation of the velocity interface, as the inverted depth of the seismic Moho showed little variation during our inversion (the black dash line in Fig. 8b). As the Moho is determined from the PmP and Pg traveltimes, and the ray density in the green dash line zone is low, the lowermost part of the crust at less than 250 km offset was not well recovered, and is rather flat in our final model (Fig. 8b, c).

The size of the cells with poor ray coverage is no greater than 30 km horizontally and 4 km in depth, as shown in the Fig. 7c. Therefore our velocity model indicates a good constraint with a resolution of 40 km by 4 km. Most of the crust of the proximal margin and the upper crust of the distal margin are well covered by rays. However, the refracted arrivals in the shallow upper mantle (Pn) are only shown in limited short offset among a few OBSs. Considering no cross reference of the Pn rays, we only extracted the Pn phases to obtain the apparent velocity of the upper mantle, but did not employ them in the velocity structure inversion. Moreover, the reflected rays (PmP) were traced along in the majority of the OBSs, indicating decent constraints from offset 50 to 430 km of the model. Thus, considering our resolution from the checkboard test, we inverted the seismic Moho undulation in relative long-wavelength. The internal crustal reflected rays (PcP) were recognized as a décollement plane within the upper crust. Due to the limited phases from the data, the reflectors are shown in short black lines from the depth of 6–8 km in the upper crust (as shown in Fig. 7c).

Discussion

Results from the wide-angle seismic inversion: the wavy crustal thickness

The profile of OBS973-3 is the first wide-angle seismic experiment performed across the northern margin of the SWSB, though a pilot experiment was conducted in 2009 at the same location but with a limitation of six OBSs (Lü

et al. 2011). A further OBS profile, “OBS Sino-French 2011 Pr1” (see Fig. 1 for location), acquired later in 2011 by the collaboration between the Guangzhou Marine Geological Survey and the Geological Laboratory of École Normale Supérieure (Pichot et al. 2014), is the only profile can be used as a comparison study with our OBS profile. We also derived the crustal thickness of several other OBS profiles that are across the margins of the SCS (Qiu et al. 2001; Yan et al. 2001; Niu et al. 2014).

However, those OBS profiles modeled with different strategies made detailed comparisons difficult. Therefore, in the profiles lacking any MCS data as constraints, we set up uniform criteria for the comparison study, including separating different layers within the crust based on our velocity model and locating the Continent-Ocean Boundary (hereafter COB) by employing stretching factor (β) estimation (Fig. 9a, b). In order to differentiate layers within the crust, we took the layer between velocity isocontours 4.0 and 5.5 km s⁻¹ as the UFL, the layer between velocity isocontours 5.5 and 6.5 km s⁻¹ as the upper-middle crust, the layer between velocity isocontours 6.5 and 6.9 km s⁻¹ as the lower crust (Rudnick and Fountain 1995) and the layer whose velocity is more than 7.0 km s⁻¹ as the high velocity layer (HVL). Though the location of the COB in the SCS has been identified by numerous papers using gravity signatures and magnetic anomalies (Taylor and Hayes 1983; Briaies et al. 1993; Braitenberg et al. 2006; Li and Song 2012; Hwang and Chang 2014), their interpretations still differ from one another. A stretching factor of about four is usually observed in the region between the completed crustal embrittlement and the onset of oceanic crust (Reston 2009), where the seaward limit of continental crust is located, and thus can be used to define the location of the COB. All the seismic profiles need to be projected along the strike of the transform faults (as shown by the dotted lines in Fig. 2) in the SWSB prior to the comparison of the stretching factor (β). Thus, we get a unified offset to the COB of the SWSB among various OBS profiles (Fig. 9a–f).

The most distinct difference between our OBS profile ‘OBS973-3’ and its adjacent one ‘OBS Sino-French Pr1’, which both went across the Zhongjian Massif in the northern margin of the SWSB, is the existence of the HVL (Fig. 9a, b). Though the HVL has been widely found in most of the northeastern SCS with a thickness of no more than 10 km, it was not treated as evidence of magma-rich margins. Instead, it has been interpreted as mafic rock from a pre-rifted relic or the post-rifting underplating (Nissen et al. 1995; Yan et al. 2001; Wang et al. 2006a). Additionally, the HVL in ‘OBS Sino-French Pr1’, with a maximum velocity of 7.7 km s⁻¹, shows a rather high-velocity gradient within 2–3 km thickness. Moreover, the possibility of serpentinization from the mantle was

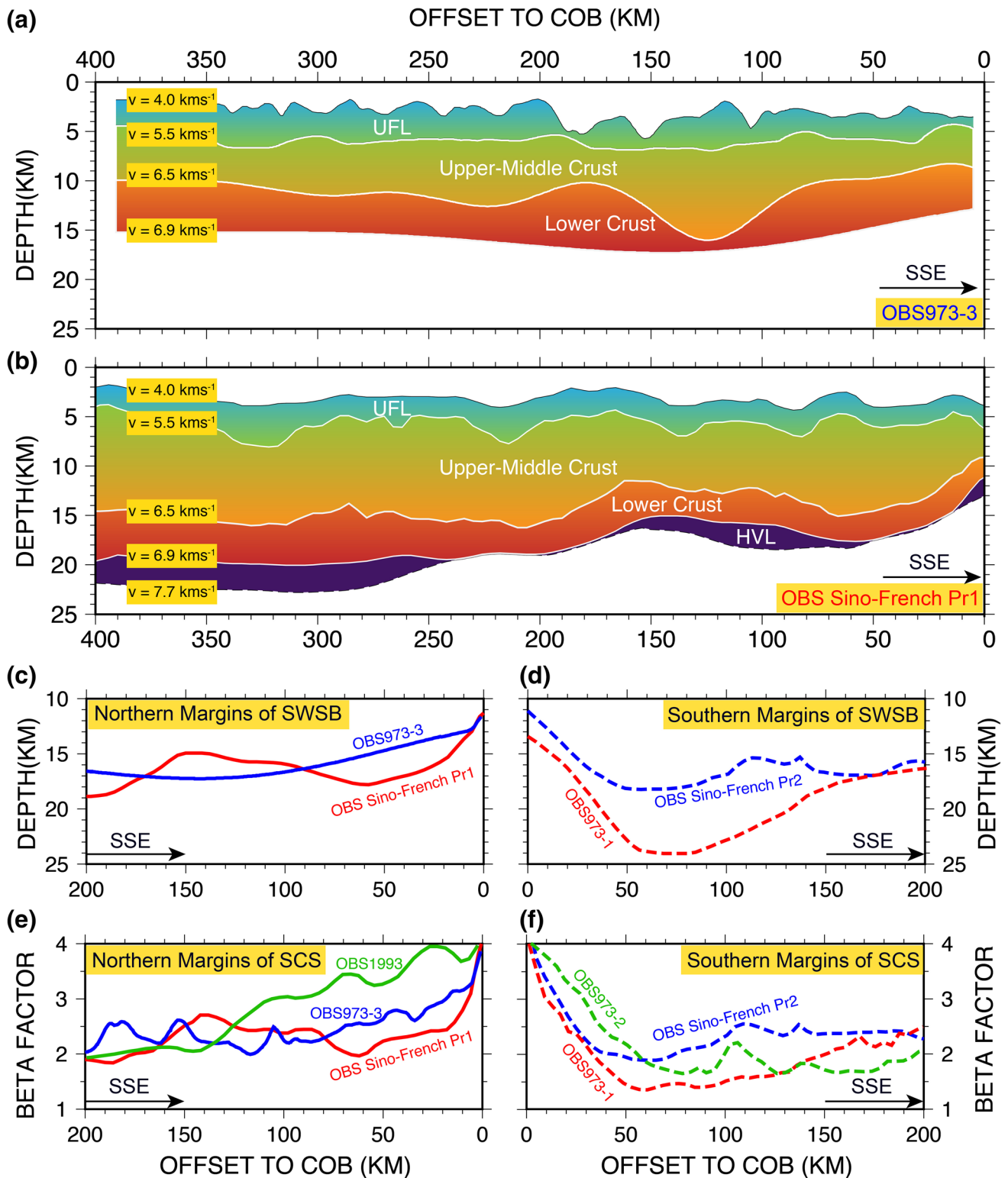


Fig. 9 Comparison of the crust structure and the stretching factors (β) from different OBS profiles located across the margins of the SCS. The data is derived from ‘OBS1993’ (Yan et al. 2001), ‘OBS973-1’ (Qiu et al. 2011), ‘OBS973-2’ (Niu et al. 2014) and ‘OBS Sino-French Pr1/Pr2’ (Pichot et al. 2014). **a** The crustal structure of ‘OBS973-3’ superimposed with velocity boundaries. **b** The crustal

structure of ‘OBS Sino-French Pr1’ superimposed with velocity boundaries. **c** The Moho depth from the profiles in the northern margin of the SWSB. **d** The Moho depth from the profiles in the southern margin of the SWSB. **e** The stretching factor (β) from the profiles in the southern margin of the SCS. **f** The stretching factor (β) from the profiles in the northern margin of the SCS

excluded considering the crustal thickness, as Pichot et al. (2014) suggested that the pre-rift relics in the lower crust resulted in the heterogeneous velocity. Regardless, one common notion for the presence of the HVL near the Moho in the SCS is that it is not related to the stretched crust associated with episodic extension in Cenozoic. In other words, it can be omitted from the measurement of the crustal extension so that it does not contribute to the stretching factor estimation for the continental margins of the SCS.

The stretching factor (β) describes how the continental crust extended during a series of tectonic events. Among all the three different methods of measuring the β -factors (Chen 2014), the crustal thickness method is the most straightforward, as long as the bias caused by the non-extension factors, such as pre-rift relic, magma underplating in the lower crust or the volcanic body intrusion in the upper crust, are removed. In our study, we used the crustal thickness from four different OBS profiles across the distal margins of the SCS, and summarized the thickness including the UFL, upper-middle crust and the lower crust to estimate the β -factors by the ratio of the thickness of the pre-rift crust to that of extended crust (McKenzie 1978). The pre-rift crustal thickness of SCS can be derived from the South China Foldbelt at the Chinese continental shelf, where the receiver function and the ambient tomography inverted the crustal thickness of around 30 km (Chen et al. 2010; Zhou et al. 2012).

Moreover, the present crustal thickness of the distal continental margins can be measured from several wide-angle seismic profiles. Compared to ‘OBS973-3’, the Moho undulation of ‘OBS Sino-French Pr1’ is rather wavier and deeper (as shown in Fig. 9a), and was the same on the southern margins as the comparison between ‘OBS Sino-French Pr1’ and ‘OBS973-1’. Given that the lithosphere break-up was diachronous along the conjugate margins of the SCS (Cullen et al. 2010) where the onset of BU varies from ~ 32 to ~ 17 Ma from the eastern to western margins (Franke et al. 2014), the western margin of the SCS experienced prolonged extension before the continental breakup. In other words, the continental rift propagating westwards is the reason that the Moho depth of ‘OBS Sino-French Pr1’ has a wavier undulation even though it locates on the same massif with ‘OBS973-3’ (as shown in the Fig. 9c, d; the profile at the west side are colored in red and the profiles at the east side are colored in blue). Another difference is the Moho depth between ‘OBS973-1’ and ‘OBS Sino-French Pr2’ on the southern margins, where the ‘OBS Sino-French Pr2’ is 6 km shallower than ‘OBS973-1’. While ‘OBS Sino-French Pr2’ is situated across the center of Zhenghe Massif, ‘OBS973-1’ is located on the edge where the crustal thinning is more efficient and the stress accumulates more quickly (Ding and Li 2016), which

might explain why ‘OBS973-1’ has a steeper Moho compared to ‘OBS Sino-French Pr2’.

Results from stretching factor comparison (β): the precipitate transition zone

Though the nature of the transition zone from continental crust to oceanic crust is still unclear in the deep margins all over the world, the intensive crustal thinning of the continent-ocean transition (hereafter COT) at the magma-poor margins often results in the exposure the serpentinized mantle and rotated fault blocks in the COT, which can be seen as an abnormal seismic velocity gradient (Reston 1996). Though there is few evidence yet of the exhumed serpentinized mantle in the SCS yet, there has been frequent speculation from the MCS profiles in the margin of the SCS (Franke et al. 2001; Cullen et al. 2010; Ding and Li 2015). In our observation, the relatively sharp velocity boundary may represent the fractured crustal rocks (Fig. 6), which represent the top basement detachment faults exhumed in the lower crust footwall. Our observation of a sharp velocity boundary is compatible with the wide-angle refraction seismic data in the Iberia-Newfoundland rifted margins (Chian et al. 1999). Thus, we used the final detachment faults as the boundary between the proximal domain and distal domain of the SWSB margins (Franke et al. 2014) by employing the definition from the Iberia-Newfoundland margins (Péron-Pinvidic and Manatschal 2009). Furthermore, this boundary correlated well with our calculated β -factors of 3.5, thus the different rift domains along the margins of the SWSB can be defined using the β -factors; the proximal domain is where β -factors vary from 2.0 to 3.5, and the distal domain is where β -factors vary from 3.5 to 4.0.

The Moho undulation of the proximal domain is relatively subdued, and most of the margins of the SWSB (Fig. 9e, f) belong to this domain, which reveals the western margins of the SCS as an ultra-wide rift feature with fewer periods of extension when compared with β -factors curves of ‘OBS1993’ from the northeastern margin (Fig. 9e). Furthermore, ‘OBS973-3’ and ‘OBS Sino-French Pr1’ from the northwestern margin show very limited the distal domain where the COT locates. Compared to ‘OBS1993’, it is less than 20 km COT, suggesting an intense rifting period before the continental breakup with the rigid blocks acting as stress accumulators for more efficient stretching. The β -factors of the northern margin are greater than the southern margin overall, which indicates that the northern margins experienced more thinning than the southern margins before the continental breakup. Moreover, the width of the necking zone (where β -factors quickly increased from 2.5 to 3.5) is quite similar, indicating that the conjugate margin shared a common rifting

history prior to the last stages of extension, though they experienced different number periods. This also might explain why there is a similar upper crustal structure where typical half graben/half host and detachment faults frequently occur along the conjugated margins of the SWSB. The β -factors of ‘OBS1993’ from the northern margin drop steadily beyond the far offset to the COB, on the contrary, the ups and downs of the β -factors in the northern margins of the SWSB reflect how the rigid blocks affected the thinning of the upper crust structure, leading to the uneven distribution of tensile stress, which also induced the sinuous shape of the COB following the opening of the SWSB.

Results from the MCS/OBS interpretation: the unresolved extension discrepancy

When the lithosphere stretching was in effect, the brittle upper crust gradually formed a half graben/half-horst structure via normal conjugate faulting, which resulted in a sequence of horizontal crustal extension. Finally, a UFL located beneath the acoustic basement formed. The fractures and subseismic deformation (Reston and McDermott 2014) within this layer are beyond the investigating depth of the MCS data, which often lead to an underestimation of the amount of stretching of upper crust using the normal faulting method. Though UFL can be imaged by the velocity anomaly from our OBS tomography, we speculated that it can only form after tens of millions years of rifting since it is seldom observed in the continental shelf of the SCS (Hu et al. 2009; Zhu et al. 2012).

Additionally, both the northern and southern margins of the SWSB have the features of an ‘outer rise’ (Lister et al. 1986) belonging to the hanging wall of the detachment fault, indicating that the extension migrated into the nearby faulted blocks, hiding the extension along the new fault block (Ranero and Pérez-Gussinyé 2010). The extension centers during several rifting stages were stayed focused in certain restricted spaces. This is an additional reason as to why the init-rift sedimentary unit from our MCS interpretation only locates in the southern margin of the SWSB and the southern tip of the Zhenghe massif.

Conclusion

In this paper, the spatial and temporal evidence of rifting across the margins of the SWSB were discussed, and the logical result of progressive extension summarized. Significant evidence is provided using a structural comparison of several seismic profiles, including the crustal stretching factor, the rigid block impact, and diachronous sedimentary units. Our major findings are as follows:

1. Seismic velocity anomaly and Moho depth in the margin of the SWSB indicate that the crust is comprised of distinct domains shaped by rifting. Prior to continental breakup, the progressive rifting center stayed focused in limited space, and rigid blocks influenced the detachment faulting that occurred in the rifting center.
2. Comparing with northern margin along the transect, the southern margin of the SWSB experienced at least one more stage of rifting, and an asymmetrical crustal rifting structure suggested an uneven distribution of tensile stress fields among the conjugate continental margins, though they might undergo a similar necking effect.
3. The refraction model showed the evidence of the existence of the upper (crustal) fracture layer (UFL). We speculate that it was the result of multi-stage extension and may lead to an underestimation of upper crustal stretching factor by the normal faulting method, which may prompt the debates over the extension discrepancy.

Acknowledgements This work was made possible by the crews of R/V SHIYAN 2 of the South China Sea Institute of Oceanology, Chinese Academy of Sciences and PI of this experiment, Dr. Xuelin Qui. We also want to give special thanks to Dr. Qingyu You for the development of the OBSs. Thanks to Dr. Barry C. Zelt for providing the seismic tracing package and Dr. James Hobro for providing the seismic tomography package. Most of the seismic processing work was performed with the Seismic Unix (SU) package of Jack Cohen and John Stockwell, and the figures in this manuscript were generated with the Generic Mapping Tool (GMT) of Paul Wessel and Walter Smith. This study was supported by the National Natural Science Foundation of China (Grants 41404050, 41476033, 41576068, 41276049, U1505232, 91428204) and the National Program on Global Change and Air-Sea Interaction (Grant GASI-GEOGE-01). The author was also supported by a fellowship of China Scholarship Council and Dr. Jian Lin while studying as a visiting graduate at the Woods Hole Oceanographic Institution, USA.

References

- Barckhausen U, Roeser H (2004) Seafloor spreading anomalies in the South China Sea revisited. *Geophys Monogr Ser* 149:121–125
- Boillot G, Recq M, Winterer EL et al (1987) Tectonic denudation of the upper mantle along passive margins: a model based on drilling results (ODP leg 103, western Galicia margin, Spain). *Tectonophysics* 132:335–342. doi:10.1016/0040-1951(87)90352-0
- Braitenberg C, Wienecke S, Wang Y (2006) Basement structures from satellite-derived gravity field: South China Sea ridge. *J Geophys Res* 111:1–15. doi:10.1029/2005JB003938
- Briaux A, Patriat P, Tapponnier P (1993) Updated Interpretation of magnetic anomalies and seafloor spreading stages in the South China Sea: implications for the Tertiary Tectonics of Southeast Asia. *J Geophys Res* 98:6299–6328. doi:10.1029/92jb02280
- Buck WR (1991) Models of continental lithospheric extension. *J Geophys Res* 96:161–178

- Chen L (2014) Stretching factor estimation for the long-duration and multi-stage continental extensional tectonics: application to the Baiyun Sag in the northern margin of the South China Sea. *Tectonophysics* 611:167–180. doi:[10.1016/j.tecto.2013.11.026](https://doi.org/10.1016/j.tecto.2013.11.026)
- Chen L, Zhong G (2008) Seismic stratigraphy analysis of the Zhongjiannan Basin in the South China Sea (in Chinese). *Geophys Prospect Pet* 47:609–616
- Chen Y, Niu F, Liu R et al (2010) Crustal structure beneath China from receiver function analysis. *J Geophys Res* 115:B03307. doi:[10.1029/2009JB006386](https://doi.org/10.1029/2009JB006386)
- Chian D, Louden KE, Minshull TA, Whitmarsh RB (1999) Deep structure of the ocean-continent transition in the southern Iberia Abyssal Plain from seismic refraction profiles: Ocean Drilling Program (Legs 149 and 173) transect. *J Geophys Res* 104:7443–7462. doi:[10.1029/1999JB900004](https://doi.org/10.1029/1999JB900004)
- Christensen NI, Mooney WD (1995) Seismic velocity structure and composition of the continental crust: a global view. *J Geophys Res* 100:9761–9788. doi:[10.1029/95jb00259](https://doi.org/10.1029/95jb00259)
- Clift P, Lin J (2001) Preferential mantle lithospheric extension under the South China margin. *Mar Pet Geol* 18:929–945. doi:[10.1016/S0264-8172\(01\)00037-X](https://doi.org/10.1016/S0264-8172(01)00037-X)
- Clift P, Lin J, Barckhausen U (2002) Evidence of low flexural rigidity and low viscosity lower continental crust during continental break-up in the South China Sea. *Mar Pet Geol* 19:951–970. doi:[10.1016/S0264-8172\(02\)00108-3](https://doi.org/10.1016/S0264-8172(02)00108-3)
- Clift PD, Lee GH, Anh Duc N et al (2008) Seismic reflection evidence for a Dangerous Grounds miniplate: no extrusion origin for the South China Sea. *Tectonics*. doi:[10.1029/2007TC002216](https://doi.org/10.1029/2007TC002216)
- Cullen A, Reemst P, Henstra G et al (2010) Rifting of the South China Sea: new perspectives. *Pet Geosci* 16:273–282. doi:[10.1144/1354-079309-908](https://doi.org/10.1144/1354-079309-908)
- Ding W, Li J (2011) Stratigraphy, tectonic structure and extension factors across the southern margin of the South China Sea: evidence from two regional multi-channel seismic. *Chin J Geophys* 54:3038–3056
- Ding W, Li J (2015) Conjugate margin pattern of the Southwest Sub-basin, South China Sea: insights from deformation structures in the continent-ocean transition zone. *Geol J*. doi:[10.1002/gj.2733](https://doi.org/10.1002/gj.2733)
- Ding W, Li J (2016) Propagated rifting in the Southwest Sub-basin, South China Sea: insights from analogue modelling. *J Geodyn*. doi:[10.1016/j.jog.2016.02.004](https://doi.org/10.1016/j.jog.2016.02.004)
- Ding W, Franke D, Li J, Steuer S (2013) Seismic stratigraphy and tectonic structure from a composite multi-channel seismic profile across the entire Dangerous Grounds, South China Sea. *Tectonophysics* 582:162–176. doi:[10.1016/j.tecto.2012.09.026](https://doi.org/10.1016/j.tecto.2012.09.026)
- Ding W, Li J, Dong C, Fang Y (2015) Oligocene-Miocene carbonates in the Reed Bank area, South China Sea, and their tectono-sedimentary evolution. *Marine Geophys Res* 36:149–165. doi:[10.1007/s11001-014-9237-5](https://doi.org/10.1007/s11001-014-9237-5)
- Falvey D, Mutter J (1981) Regional plate tectonics and the evolution of Australia's passive continental margins. *BMR J Aust Geol Geophys* 6:1–29
- Franke D (2013) Rifting, lithosphere breakup and volcanism: comparison of magma-poor and volcanic rifted margins. *Mar Pet Geol* 43:63–87. doi:[10.1016/j.marpetgeo.2012.11.003](https://doi.org/10.1016/j.marpetgeo.2012.11.003)
- Franke D, Hinz K, Oncken O (2001) The Laptev Sea Rift. *Mar Pet Geol* 18:1083–1127. doi:[10.1016/S0264-8172\(01\)00041-1](https://doi.org/10.1016/S0264-8172(01)00041-1)
- Franke D, Barckhausen U, Baristean N et al (2011) The continent-ocean transition at the southeastern margin of the South China Sea. *Mar Pet Geol* 28:1187–1204. doi:[10.1016/j.marpetgeo.2011.01.004](https://doi.org/10.1016/j.marpetgeo.2011.01.004)
- Franke D, Savva D, Pubellier M et al (2014) The final rifting evolution in the South China Sea. *Mar Pet Geol* 58:704–720. doi:[10.1016/j.marpetgeo.2013.11.020](https://doi.org/10.1016/j.marpetgeo.2013.11.020)
- Hall R (2002) Cenozoic geological and plate tectonic evolution of SE Asia and the SW Pacific: computer-based reconstructions, model and animations. *J Asian Earth Sci* 20:353–431. doi:[10.1016/S1367-9120\(01\)00069-4](https://doi.org/10.1016/S1367-9120(01)00069-4)
- Hall R (2009) Hydrocarbon basins in SE Asia: understanding why they are there. *Pet Geosci* 15:131–146. doi:[10.1144/1354-079309-830](https://doi.org/10.1144/1354-079309-830)
- Hobro JWD, Singh SC, Minshull TA (2003) Three-dimensional tomographic inversion of combined reflection and refraction seismic traveltimes. *Geophys J Int* 152:79–93. doi:[10.1046/j.1365-246X.2003.01822.x](https://doi.org/10.1046/j.1365-246X.2003.01822.x)
- Hu D, Zhou D, Wu X et al (2009) Crustal structure and extension from slope to deepsea basin in the northern South China Sea. *J Earth Sci* 20:27–37. doi:[10.1007/s12583-009-0003-6](https://doi.org/10.1007/s12583-009-0003-6)
- Huisman RS, Beaumont C (2008) Complex rifted continental margins explained by dynamical models of depth-dependent lithospheric extension. *Geology* 36:163–166. doi:[10.1130/G24231A.1](https://doi.org/10.1130/G24231A.1)
- Hutchison CS (2004) Marginal basin evolution: the southern South China Sea. *Mar Pet Geol* 21:1129–1148
- Hutchison CS, Vijayan VR (2010) What are the Spratly Islands? *J Asian Earth Sci* 39:371–385. doi:[10.1016/j.jseae.2010.04.013](https://doi.org/10.1016/j.jseae.2010.04.013)
- Hwang C, Chang ETY (2014) Geophysics. Seafloor secrets revealed. *Science* 346:32–33. doi:[10.1126/science.1260459](https://doi.org/10.1126/science.1260459)
- Li C-F, Song T (2012) Magnetic recording of the Cenozoic oceanic crustal accretion and evolution of the South China Sea basin. *Chin Sci Bull* 57:3165–3181. doi:[10.1007/s11434-012-5063-9](https://doi.org/10.1007/s11434-012-5063-9)
- Li C-F, Wang P, Franke D et al (2012a) Scientific drilling. *Sci Drill*. doi:[10.2204/iodp.sd.14.07.2012](https://doi.org/10.2204/iodp.sd.14.07.2012)
- Li J, Ding W, Wu Z et al (2012b) The propagation of seafloor spreading in the southwestern subbasin, South China Sea. *Chin Sci Bull* 57:3182–3191. doi:[10.1007/s11434-012-5329-2](https://doi.org/10.1007/s11434-012-5329-2)
- Li C-F, Xu X, Lin J et al (2014) Ages and magnetic structures of the South China Sea constrained by deep tow magnetic surveys and IODP Expedition 349. *Geochem Geophys Geosyst* 15:4958–4983. doi:[10.1002/2014GC005567](https://doi.org/10.1002/2014GC005567)
- Li C-F, Li J, Ding W et al (2015a) Seismic stratigraphy of the central South China Sea basin and implications for neotectonics. *J Geophys Res* 120:1377–1399. doi:[10.1002/2014JB011686](https://doi.org/10.1002/2014JB011686)
- Li C-F, Lin J, Kulhanek DK et al (2015b) Site U1433. In: *Proceedings of the international ocean discovery program*, vol 349
- Lister GS, Etheridge MA, Symonds PA (1986) Detachment faulting and the evolution of passive continental margins. *Geology* 14:246–250. doi:[10.1130/0091-7613\(1986\)14<246:dfateo>2.0.co;2](https://doi.org/10.1130/0091-7613(1986)14<246:dfateo>2.0.co;2)
- Lü C, Hao T, Qiu X et al (2011) Deep crustal structure of the northern part of southwest sub-basin, South China Sea, from ocean bottom seismic data. *Chin J Geophys* 54:1022–1032. doi:[10.1002/cjg2.1681](https://doi.org/10.1002/cjg2.1681)
- Lü C, Yao Y, Wu S, Dong D (2013) Formation and syn-rifting process of the Wan'an Basin, South China Sea. *Chin J Oceanol Limnol* 31:190–201
- McIntosh K, Nakamura Y, Wang T-K et al (2005) Crustal-scale seismic profiles across Taiwan and the western Philippine Sea. *Tectonophysics* 401:23–54. doi:[10.1016/j.tecto.2005.02.015](https://doi.org/10.1016/j.tecto.2005.02.015)
- McKenzie D (1978) Some remarks on the development of sedimentary basins. *Earth Planet Sci Lett* 40:25–32. doi:[10.1016/0012-821x\(78\)90071-7](https://doi.org/10.1016/0012-821x(78)90071-7)
- Mooney WD, Laske G, Masters TG (1998) CRUST 5.1: A global crustal model at 5° × 5°. *J Geophys Res Solid Earth* 103:727–747. doi:[10.1029/97JB02122](https://doi.org/10.1029/97JB02122)
- Morley CK (2016) Major unconformities/termination of extension events and associated surfaces in the South China Seas: review and implications for tectonic development. *J Asian Earth Sci* 120:62–86. doi:[10.1016/j.jseae.2016.01.013](https://doi.org/10.1016/j.jseae.2016.01.013)

- Nissen SS, Hayes DE, Buhl P et al (1995) Deep penetration seismic soundings across the northern margin of the South China Sea. *J Geophys Res* 100:22407–22433. doi:[10.1029/95jb01866](https://doi.org/10.1029/95jb01866)
- Niu X-W, Wei X-D, Ruan A-G, Wu Z-L (2014) Comparison of inversion method of wide-angle Ocean Bottom Seismometer profile a case study of profile OBS973-2 across Liyue bank in the South China Sea. *Chin J Geophys* 57:2701–2712. doi:[10.6038/cjg20140828](https://doi.org/10.6038/cjg20140828)
- Péron-Pinvidic G, Manatschal G (2009) The final rifting evolution at deep magma-poor passive margins from Iberia-Newfoundland: a new point of view. *Int J Earth Sci* 98:1581–1597. doi:[10.1007/s00531-008-0337-9](https://doi.org/10.1007/s00531-008-0337-9)
- Pichot T, Delescluse M, Chamot-Rooke N et al (2014) Deep crustal structure of the conjugate margins of the SW South China Sea from wide-angle refraction seismic data. *Mar Pet Geol* 58:627–643. doi:[10.1016/j.marpetgeo.2013.10.008](https://doi.org/10.1016/j.marpetgeo.2013.10.008)
- Qiu X, Ye S, Wu S et al (2001) Crustal structure across the Xisha Trough, northwestern South China Sea. *Tectonophysics* 341:179–193. doi:[10.1016/s0040-1951\(01\)00222-0](https://doi.org/10.1016/s0040-1951(01)00222-0)
- Qiu X, Zhao M, Ao W et al (2011) OBS survey and crustal structure of the Southwest Sub-basin and Nansha Block, South China Sea. *Chin J Geophys* 54:1009–1021
- Ranero CR, Pérez-Gussinyé M (2010) Sequential faulting explains the asymmetry and extension discrepancy of conjugate margins. *Nature* 468:294–299. doi:[10.1038/nature09520](https://doi.org/10.1038/nature09520)
- Reston TJ (1996) The S reflector west of Galicia: the seismic signature of a detachment fault. *Geophys J Int* 127:230–244. doi:[10.1111/j.1365-246X.1996.tb01547.x](https://doi.org/10.1111/j.1365-246X.1996.tb01547.x)
- Reston T (2007) Extension discrepancy at North Atlantic nonvolcanic rifted margins: depth-dependent stretching or unrecognized faulting? *Geology* 35:367. doi:[10.1130/G23213A.1](https://doi.org/10.1130/G23213A.1)
- Reston TJ (2009) The structure, evolution and symmetry of the magma-poor rifted margins of the North and Central Atlantic: a synthesis. *Tectonophysics* 468:6–27. doi:[10.1016/j.tecto.2008.09.002](https://doi.org/10.1016/j.tecto.2008.09.002)
- Reston TJ, McDermott KG (2011) Successive detachment faults and mantle unroofing at magma-poor rifted margins. *Geology* 39:1071–1074. doi:[10.1130/G32428.1](https://doi.org/10.1130/G32428.1)
- Reston T, McDermott K (2014) An assessment of the cause of the “extension discrepancy” with reference to the west Galicia margin. *Basin Res* 26:135–153. doi:[10.1111/bre.12042](https://doi.org/10.1111/bre.12042)
- Ru K, Pigott JD (1986) Episodic rifting and subsidence in the South China Sea. *AAPG Bull* 70:1136–1155
- Ruan A, Niu X, Qiu X et al (2011) A wide angle ocean bottom seismometer experiment across Liyue Bank, the southern margin of the South China Sea. *Chin J Geophys* 54:1033–1044. doi:[10.1002/cjg2.1682](https://doi.org/10.1002/cjg2.1682)
- Rudnick RL, Fountain DM (1995) Nature and composition of the continental crust: a lower crustal perspective. *Rev Geophys* 33:267–309. doi:[10.1029/95RG01302](https://doi.org/10.1029/95RG01302)
- Savva D, Pubellier M, Franke D et al (2014) Different expressions of rifting on the South China Sea margins. *Mar Pet Geol* 58:579–598. doi:[10.1016/j.marpetgeo.2014.05.023](https://doi.org/10.1016/j.marpetgeo.2014.05.023)
- Schlüter HU, Hinz K, Block M, Schlüter HU (1996) Tectono-stratigraphic terranes and detachment faulting of the South China Sea and Sulu Sea. *Mar Geol* 130:39–78. doi:[10.1016/0025-3227\(95\)00137-9](https://doi.org/10.1016/0025-3227(95)00137-9)
- Shaw PR, Orcutt JA (1985) Waveform inversion of seismic refraction data and applications to young Pacific crust. *Geophys J Roy Astron Soc* 82:375–414. doi:[10.1111/j.1365-246X.1985.tb05143.x](https://doi.org/10.1111/j.1365-246X.1985.tb05143.x)
- Shi X, Burov E, Leroy S et al (2005) Intrusion and its implication for subsidence: a case from the Baiyun Sag, on the northern margin of the South China Sea. *Tectonophysics* 407:117–134. doi:[10.1016/j.tecto.2005.07.004](https://doi.org/10.1016/j.tecto.2005.07.004)
- Sibuet J-C, Yeh Y-C, Lee C-S (2016) Geodynamics of the South China Sea. *Tectonophysics*. doi:[10.1016/j.tecto.2016.02.022](https://doi.org/10.1016/j.tecto.2016.02.022)
- Song T, Li C-F (2015) Rifting to drifting transition of the Southwest Subbasin of the South China Sea. *Mar Geophys Res* 36:167–185. doi:[10.1007/s11001-015-9253-0](https://doi.org/10.1007/s11001-015-9253-0)
- Steuer S, Franke D, Meresse F et al (2014) Oligocene-Miocene carbonates and their role for constraining the rifting and collision history of the Dangerous Grounds, South China Sea. *Mar Pet Geol* 58:644–657. doi:[10.1016/j.marpetgeo.2013.12.010](https://doi.org/10.1016/j.marpetgeo.2013.12.010)
- Sun F, Wang Z, Hao T (2011) Seismic imaging of complicated deep structures in southern South China Sea. *Chin J Geophys* 54:3210–3216
- Taylor B, Hayes DE (1983) Origin and history of the South China Sea basin. In: Hayes DE (ed) *The tectonic and geologic evolution of Southeast Asian seas and islands: part 1*, 1st edn. American Geophysical Union, Washington, DC, pp 23–56
- Tucholke BE, Sawyer DS, Sibuet J-C (2007) Breakup of the Newfoundland-Iberia rift. *Geol Soc Lond Spec Publ* 282:9–46. doi:[10.1144/SP282.2](https://doi.org/10.1144/SP282.2)
- Wang TK, Chen M-K, Lee C-S, Xia K (2006a) Seismic imaging of the transitional crust across the northeastern margin of the South China Sea. *Tectonophysics* 412:237–254. doi:[10.1016/j.tecto.2005.10.039](https://doi.org/10.1016/j.tecto.2005.10.039)
- Wang Y-T, Chen L, Wu D-M (2006b) Velocity data analysis and its application to Zhongjiannan Basin in South China Sea (in Chinese). *J Trop Oceanogr* 25:49–55
- Wang Q, Qiu X-L, Ming-Hui Z et al (2016) Analysis and processing on abnormal OBS data in the South China Sea (in Chinese with English abstract). *Chin J Geophys* 59:1102–1112. doi:[10.6038/cjg20160330](https://doi.org/10.6038/cjg20160330)
- Wernicke B (1981) Low-angle normal faults in the Basin and Range Province: nappe tectonics in an extending orogen. *Nature* 291:645–648
- White RS, Smith LK (2009) Crustal structure of the Hatton and the conjugate east Greenland rifted volcanic continental margins, NE Atlantic. *J Geophys Res* 114:B02305. doi:[10.1029/2008JB005856](https://doi.org/10.1029/2008JB005856)
- Whitmarsh RB, Manatschal G, Minshull TA (2001) Evolution of magma-poor continental margins from rifting to seafloor spreading. *Nature* 413:150–154
- Yan P, Liu H (2004) Tectonic-stratigraphic division and blind fold structures in Nansha Waters, South China Sea. *J Asian Earth Sci* 24:337–348. doi:[10.1016/j.jseas.2003.12.005](https://doi.org/10.1016/j.jseas.2003.12.005)
- Yan P, Zhou D, Liu Z (2001) A crustal structure profile across the northern continental margin of the South China Sea. *Tectonophysics* 338:1–21. doi:[10.1016/s0040-1951\(01\)00062-2](https://doi.org/10.1016/s0040-1951(01)00062-2)
- Yan Q, Shi X, Castillo PR (2014) The late Mesozoic–Cenozoic tectonic evolution of the South China Sea: a petrologic perspective. *J Asian Earth Sci* 85:178–201. doi:[10.1016/j.jseas.2014.02.005](https://doi.org/10.1016/j.jseas.2014.02.005)
- Yao Y, Liu H, Yang C et al (2012) Characteristics and evolution of Cenozoic sediments in the Liyue Basin, SE South China Sea. *J Asian Earth Sci* 60:114–129. doi:[10.1016/j.jseas.2012.08.003](https://doi.org/10.1016/j.jseas.2012.08.003)
- Zelt CA (1999) Modelling strategies and model assessment for wide-angle seismic traveltimes data. *Geophys J Int* 139:183–204. doi:[10.1046/j.1365-246X.1999.00934.x](https://doi.org/10.1046/j.1365-246X.1999.00934.x)
- Zelt CA, Forsyth DA (1994) Modeling wide-angle seismic data for crustal structure: southeastern Grenville Province. *J Geophys Res* 99:11687–11704. doi:[10.1029/93jb02764](https://doi.org/10.1029/93jb02764)
- Zelt CA, Sain K, Naumenko JV, Sawyer DS (2003) Assessment of crustal velocity models using seismic refraction and reflection tomography. *Geophys J Int* 153:609–626. doi:[10.1046/j.1365-246X.2003.01919.x](https://doi.org/10.1046/j.1365-246X.2003.01919.x)
- Zhao C-Y, Song H-B, Li J-B, Song Y (2011) Tectonic and seismic interpretation of line NH973-1 along southwest sub-basin in

- South China Sea (in Chinese). *Chin J Geophys* 54:3258–3268. doi:[10.3969/j.issn.0001-5733.2011.12.024](https://doi.org/10.3969/j.issn.0001-5733.2011.12.024)
- Zhou L, Xie J, Shen W et al (2012) The structure of the crust and uppermost mantle beneath South China from ambient noise and earthquake tomography. *Geophys J Int* 189:1565–1583. doi:[10.1111/j.1365-246X.2012.05423.x](https://doi.org/10.1111/j.1365-246X.2012.05423.x)
- Zhu J, Qiu X, Kopp H et al (2012) Shallow anatomy of a continent–ocean transition zone in the northern South China Sea from multichannel seismic data. *Tectonophysics* 554–557:18–29. doi:[10.1016/j.tecto.2012.05.027](https://doi.org/10.1016/j.tecto.2012.05.027)